Relation between the Infrared Spectra and the Lateral Specific Surface Areas of Gibbsite Samples

ARTICLE *in* LANGMUIR · JUNE 2000

Impact Factor: 4.46 · DOI: 10.1021/la000098v

3 AUTHORS, INCLUDING:

Nsoki Phambu
Tennessee State University
10 PUBLICATIONS **104** CITATIONS

Relation between the Infrared Spectra and the Lateral Specific Surface Areas of Gibbsite Samples

Nsoki Phambu, Bernard Humbert,* and Andre Burneau

Laboratoire de Chimie-Physique pour l'Environnement, UMR CNRS−UHP 7564, 405 rue de Vandoeuvre, 54 600 Villers-lès-Nancy, France

Received January 25, 2000. In Final Form: April 20, 2000

The chemical behavior of crystalline $Al(OH)_3$ samples is governed by the lateral-to-basal surface ratio. For well-crystallized gibbsite samples possessing the two types of surfaces clearly spatially separated, a vibrational component at ∼3460 cm^{-1} in the infrared absorption spectra, not displayed in the Raman spectra, increases linearly with the lateral specific area determined by a gas adsorption isotherm. This intense and broad line is related to hydroxyl stretching modes of $AlOH_2^{1/2+}$ or $AlOH^{1/2-}$ species present on the edge faces. However, it is too simplistic to assign this band to a mode of one or the other of these species. More complex structures combining both species should also be considered. When an evacuated sample is submitted during a short time to a D_2O vapor injection, the OD spectral region displays essentially one broad component at 2563 cm^{-1}, corresponding to the 3460 cm^{-1} band in the OH region and not to the other modes of the bulk hydroxyls. This experimental observation is also in agreement with the assignment of this infrared band to reactive superficial species.

Introduction

At the solid/solution or air interfaces of metal (hydr)-oxides, several types of chemical groups exist, as has been frequently observed in infrared studies.[1−4] Each of these groups will react according to its own affinity for protons in aqueous solutions, i.e., its proton affinity constant. This constant depends on many factors, e.g., the valence of the cation (M), its electron configuration, and the M−H distance of the reacting surface group.[5,6] Besides these factors, the number of surrounding ligands, the number of central cations coordinating with a ligand, and the type of reacting ligand can also influence the proton affinity constant.[5−8] Aluminum hydroxides are frequently found in soils as independent particles or as coatings on minerals. Gibbsite can be considered, in a first approximation, as the crystalline representative of this important group of aluminum hydroxides.[9] Due to its morphology, a gibbsite crystal displays two types of surfaces with different proton affinities. The gibbsite structure is characterized by aluminum ions in hexacoordination with hydroxyls. The Al^{3+} ions distribute their charge over six surrounding hydroxyls, neutralizing on the average half of a unit charge per Al−OH bond ($v = {}^1/_2$). Two aluminum ions are needed to neutralize one OH^- ion in the gibbsite structure. Thus, in the volume of the crystal, the hydroxyls are all doubly coordinated. The same holds for the OH^- ions at the planar faces of the mineral, the (001) faces. At the edge faces, two kinds of surface groups are present: singly and doubly coordinated hydroxyls. The singly coordinated hydroxyl can be expressed as either $AlOH^{1/2-}$ or $AlOH_2^{1/2+}$. In aqueous solution, an equilibrium between the two forms exists:[10]

$$AlOH^{1/2-} + H^+_S \leftrightarrow AlOH_2^{1/2+}$$

where H^+_S is the proton form near the plane of adsorption with the intrinsic proton association constant K_{12}. The log K_{12} value is close to 10.[5,8,9] Usually, only singly coordinated $AlOH^{1/2-}$ and $AlOH_2^{1/2+}$ groups are present, since the first protonation constant of a singly coordinated group is extremely high.[5]

Doubly coordinated Al_2OH groups can be protonated at very low pH values and can be dissociated at very high pH values, forming oxo surface species:

$$Al_2O^- + H^+_S \leftrightarrow Al_2OH \qquad \log K_{21} = 12.3$$

$$Al_2OH + H^+_S \leftrightarrow Al_2OH_2^+ \qquad \log K_{22} = -1.5$$

The planar faces of a dried gibbsite sample have only Al_2OH^0 groups whereas the edge faces have either Al_2OH^0 groups or $AlOH^{1/2-}$ and $AlOH_2^{1/2+}$ groups. For electric neutrality of the dried solid without counterions at the surface, there are as many $AlOH^{1/2-}$ groups as $AlOH_2^{1/2+}$ groups.

This last point was never taken into account in the previous vibrational spectroscopic studies of the aluminum hydroxides. However, the published infrared spectra of either bayerite powder or gibbsite powder are not totally similar from one paper to another.[11−21] In particular,

(1) Peri, J. B. *J. Phys. Chem.* **1965**, *69*, 220.
(2) Jones, P.; Hockey, J. A. *Trans. Faraday Soc.* **1971**, *67*, 2679.
(3) Parfitt, L. R.; Atkinson, R. J.; Smart, P. St. C. *Soil Sci. Soc. Am. Proc.* **1975**, *39*, 837.
(4) Lewis, D. G.; Farmer, V. C. *Clay Miner.* **1986**, *21*, 93.
(5) Hiemstra, T.; Van Riemsdijk, W. H.; Bolt, G. H. *J. Colloid Interface Sci.* **1989**, *133*, 91.
(6) Hiemstra, T.; De Wit, J. C. M.; Van Riemsdijk, W. H. *J. Colloid Interface Sci.* **1989**, *133*, 105.
(7) Kawakami, H.; Yoshida, S. *J. Chem. Soc., Faraday Trans. 2* **1985**, *81*, 1117.
(8) Hiemstra, T.; Van Riemsdijk, W. H.; Bruggenwert, M. G. M. *Neth. J. Agric. Sci.* **1987**, *35*, 281.
(9) Hiemstra, T.; Yong, H.; Van Riemsdijk, W. H. *Langmuir* **1999**, *15*, 5942.
(10) Bolt, G. H.; Van Riemsdijk, W. H. In *Soil Chemistry. B. Physico-Chemical Models*, 2nd ed.; Bolt, G. H., Ed.; Elsevier: Amsterdam, 1982; p 459.
(11) Kolesova, V. A.; Ryskin, I. A. *Opt. Spectrosc.* **1959**, *7*, 165.
(12) Takamura, T.; Koezuka, J. *Nature* **1965**, *207*, 965.
(13) Weismiller, R. A.; Ahlrichs, J. L.; White, J. L. *Soil Sci. Soc. Am. Proc.* **1967**, *31*, 459.
(14) Rouquerol, J.; Fraissard, J.; Mathieu, M. V.; Elston, J.; Inelik, B. *Bull. Soc. Chim. Fr.* **1970**, *12*, 4233.
(15) Elderfield, H.; Hem, J. D. *Miner. Mag.* **1973**, *39*, 89.
(16) Vivien, D.; Stegmann, M. C.; Mazières, C. *J. Chim. Phys. Phys.-Chim. Biol.* **1973**, *70*, 1502.

10.1021/la000098v CCC: $19.00
Published on Web 06/27/2000

between 3420 and 3490 cm^{-1}, a component at about 3470 cm^{-1} is more or less intense in the infrared spectra, while the Raman spectra display no such component. Moreover, Takamura et al.[12] showed that the absorption band at 3460 cm^{-1} was increased by a grinding effect on hydrargillite samples. Their interpretation was that these powdering effects were not due to any increase in the surface groups but were due more likely to crystal deformation by mechanical stress during the grinding.[12] N.P. experimentally observed the same phenomenon.[22] However, he also showed that, for many other chemically synthesized samples, this component was present directly after synthesis without any mechanical stress on the samples.[22,23]

The objective of this paper is to present and analyze a series of experimental results obtained for a set of gibbsite samples. For each sample, a multidisciplinary approach was used, including infrared absorption spectroscopy, Raman scattering spectrometry, scanning electron microscopy, and gas adsorption isotherms. The latter were analyzed with the rapid method established by Villièras et al., based on the summation of local-derivative isotherms.[24,25] We examine the entire set of complementary results in order to provide another possible assignment for the absorbance component at 3460 cm^{-1}.

Experimental Section

Materials. Four samples were identified as gibbsite crystals from their X-ray diffractograms and their infrared/Raman spectra. Three of these four samples (noted A, B, and C) were prepared by precipitation of a sodium aluminate solution effected by decreasing the pH, while the fourth sample (D) was prepared at acid pH from an oversaturated aluminum solution in which Al_{13} polycations were initially the essential species.

The latter gibbsite sample was obtained by hydrolysis of an $AlCl_3 \cdot 6H_2O$ solution.[26] The first step was the synthesis of an Al_{13} polycation, the structure of which comprised 12 aluminum octahedrons surrounding a central aluminum tetrahedron. This polycation was obtained by slow NaOH hydrolysis of $AlCl_3 \cdot 6H_2O$ under vigorous stirring, up to an Na/Al ratio of 2.2; the final pH was close to 4.5. The solution, at this time, contained 95% of the aluminum in the form of Al_{13}. The second step consisted of dialyzing a 10^{-1} M Al_{13} solution against deionized water using a Spectrapo 3500 dialysis bag.[23] During the dialysis, exchange of the chloride counterions due to hydrolysis by water resulted in the precipitation of $Al(OH)_3$ inside the bag. The dialysis was stopped when the water outside the bag was free of Cl^-. The duration of the dialysis was 3 weeks. The obtained precipitate was then rinsed and freeze-dried.

The three other samples were precipitated from a sodium aluminate solution prepared by a basic attack on pure metallic aluminum (purity 99.9%; provided by Péchiney). The reaction balance of this oxidation of aluminum is

$$2Al + 2OH^- + 6H_2O \leftrightarrow 2Al(OH)_4^- + 3H_2 \quad (1)$$

The precipitation of gibbsite is written

$$Al(OH)_4^-(aq) \leftrightarrow Al(OH)_3(gib) + OH^-(aq) \quad (2)$$

The overall balance for reactions 1 and 2 is

$$2Al^0(s) + 6H_2O(l) = 2Al(OH)_3(gib) + 3H_2(g) \quad (3)$$

Because of the very large value of $\log K_3 (=153)$, the aluminum oxidation according to reaction 3 should be thermodynamically complete when H_2 evolves from the system, even if the initial $OH^-/Al^0(s)$ ratio, R, is smaller than 1. It was found, however, that a highly basic medium with a large R kinetically favored the precipitation of pure gibbsite over other poly types of aluminum hydroxide. But it was also found from equilibrium conditions for reaction 2, whose $\log K_2 = 0.12$, that R should not be too high. By calling C the initial OH^- concentration and ζ the amount of precipitated gibbsite per liter and writing K_2 as a concentration ratio at equilibrium, that is

$$K_2 = \frac{[OH^-]}{[Al(OH)_4^-]}$$

because the activity coefficients of both monovalent anions should be similar, we find that

$$K_2 = \frac{C(1 - 1/R) + \zeta}{C/R - \zeta}$$

From this relation, it appears that the precipitation of gibbsite is possible for $R < 1 + K_2 = 2.32$. In practice, we used $C = 3$ M and $R > 2.1$ for the aluminum attack. When necessary, the effective value of R was further decreased by acidification of the solution.[22] This acidification step corresponding to

$$Al(OH)_4^-(aq) + H_3O^+(aq) \leftrightarrow Al(OH)_3(gib) + H_2O(l)$$

allowed the precipitation of a pure gibbsite phase. The precipitate was then rinsed several times and dried.[22] No traces of Na^+ or CO_3^{2-} and HCO_3^- were displayed respectively in the X-ray photoelectron spectra or the infrared spectra of our dried and rinsed samples.[22]

Characterization Methods. *Infrared Spectroscopy.* The infrared spectra were obtained with a Fourier transform infrared spectrometer device, Perkin-Elmer System 2000. An easy and rapid characterization was obtained by collecting the diffuse reflectance spectrum of the sample mixed with KBr at 3% by weight with Harrick DRA-3XX-PE9 and HVC.DRP optical devices. The spectral resolution was 4 cm^{-1}. For quantitative analysis, infrared spectra were obtained for pellets containing 1 mg of sample mixed with 250 mg of KCl. Each disk had a diameter either of 13 or 25 mm and was obtained under a pressure of 10 MPa. The detector used was a broad-band DTGS. To avoid excessively large infrared absorptions of physically adsorbed water, the disks were stored for 3 days with either a silica gel or a P_2O_5 powder in a hermetically sealed cell. This procedure was essential to acquiring transmitted infrared spectra with sufficiently good baselines in the 3000−4000 cm^{-1} spectral range to quantify and decompose the absorption components.

Raman Spectrometry. Raman spectra were recorded with a triple-subtractive-monochromator Jobin Yvon T64000 spectrometer equipped with a confocal microscope. The detector was a charged-coupled device (CCD) cooled by liquid nitrogen. The Raman spectra were excited by a laser beam at 514.53 nm emitted by an argon laser (Stabilite 2017, Spectra Physics), focused on the samples with a diameter of about 1.5 μm and a power of about 20 mW. The Raman backscattering was collected through the microscope objective (×50) and dispersed by an 1800 groove/mm grating to obtain 2.7 cm^{-1} spectral resolution. The precision of the wavenumber in a vacuum was better than 0.8 cm^{-1}.

(17) Mardilovich, P. P.; Trokimets, A. I. *Appl. Spectrosc.* **1982**, *36*, 258.
(18) Hsu, P. H. In *Minerals in Soil Environments*, 2nd ed.; Dixon, J. B., Weed, S. B., Eds.; Soil Science Society of America: Madison, WI, 1989; p 331.
(19) Rodgers, K. A.; Gregory, M. R.; Cooney, R. P. *Clay Miner.* **1989**, *24*, 531.
(20) Highfield, J. G.; Boewen, P. *Anal. Chem.* **1989**, *61*, 2399.
(21) Namkung, J. S.; Hoke, M.; Rogowski, R. S.; Albin, S. *Appl. Spectrosc.* **1995**, *49*, 1305.
(22) Phambu, N. Préparation d'hydroxydes d'aluminium. Thesis, University of Nancy, France, 1997.
(23) Molis, E.; Barrès, O.; Marchand, H.; Humbert, B.; Thomas, F. *Colloids Surf., A*, in press.
(24) Villièras, F.; Cases, J. M.; Francois, M.; Michot, L. J.; Thomas, F. *Langmuir* **1992**, *8*, 1789.
(25) Villièras, F.; Michot, L. J.; Bardot, F.; Cases, J. M.; Francois, M.; Rudzinski, W. *Langmuir* **1997**, *13*, 11104.
(26) Gastucheand, M. C.; Herbillon, A. *Bull. Soc. Chim. Fr.* **1962**, *243*, 1404.

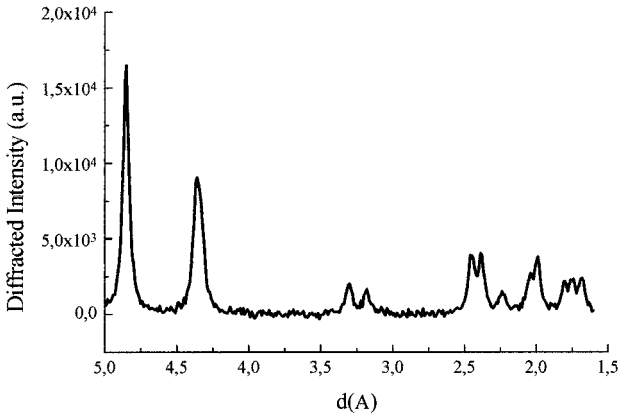

Figure 1. X-ray diffractogram of sample B. The measured diffracted lines are reported in Table 1.

Table 1. X-ray Diffraction Data for $Al(OH)_3$ Crystals and for Our Samples[a]

gibbsite					our samples	
ref 14	ref 17	ref 26	bayerite[27]	norstrandite[14,26]	A−C	D
4.85 (100)	4.85	4.82 (100)			4.82	4.85
				4.79 (100)		
			4.71 (100)			
4.37 (40)	4.37	4.32 (80)	4.35 (100)	4.32 (12)	4.37	4.35
4.31 (20)	4.32				4.33	
				4.21 (10)		
3.31 (10)	3.31	3.30 (10)			3.31	3.29
3.18 (7)	3.18	3.19 (10)	3.20 (20)		3.18	3.19
2.45 (15)	2.45	2.43 (20)			2.45	2.46
	2.38	2.39 (20)		2.39 (9)	2.38	2.39
				2.26 (15)		
2.17 (8)	2.24	2.15 (5)	2.22 (60)		2.24	2.18
2.04 (15)	2.04	2.03 (10)		2.02 (8)	2.04	2.05
	1.99	1.97 (10)			1.99	1.99
		1.91 (10)		1.90 (8)		
1.80 (10)	1.80	1.79 (5)			1.80	1.79
1.75 (9)	1.75	1.74 (5)	1.72 (20)		1.75	1.75
1.69 (7)	1.68	1.68 (5)			1.68	1.68
1.46 (8)		1.44 (10)	1.46 (8)			

[a] Values given in parentheses are the percents of the intensities of the diffracted lines.

X-ray Diffraction. The crystallographic characteristics were obtained with the Debye−Sherrer method using a Philipps X-ray diffractometer with the Cu $K\alpha_1$ line at 1.5406 Å.

Scanning Electron Microscopy. The sizes and shapes of the analyzed particles were visualized by a Hitachi S-2500 scanning electron microscope, equipped with a LaB6 canon and working under a vacuum of 10^{-6} mbar. The spatial resolution was estimated at about 25 Å.

Specific Area Determinations. The specific surface areas were estimated from krypton adsorption−desorption isotherms at 77 K using step-by-step volumetric analysis on homemade equipment after outgassing of the samples at 100 °C. Any structural changes are not displayed on the infrared spectra as long as the outgassing temperature is kept lower than 130 °C.

Results and Discussion

Characterization of the Crystal Structures of Gibbsite Samples. The four samples display the same X-ray powder diffraction pattern (Figure 1 and Table 1). The reflection lines correspond closely to those of gibbsite reported previously in the literature.[27−29] Samples A−C display X-ray diffractograms with narrow widths characteristic of grain sizes larger than 100 nm. Only for the sample D are the lines broader. The grain size of this last sample is about 13 nm if the coherent thickness given by the Sherrer equation is identified with the size.

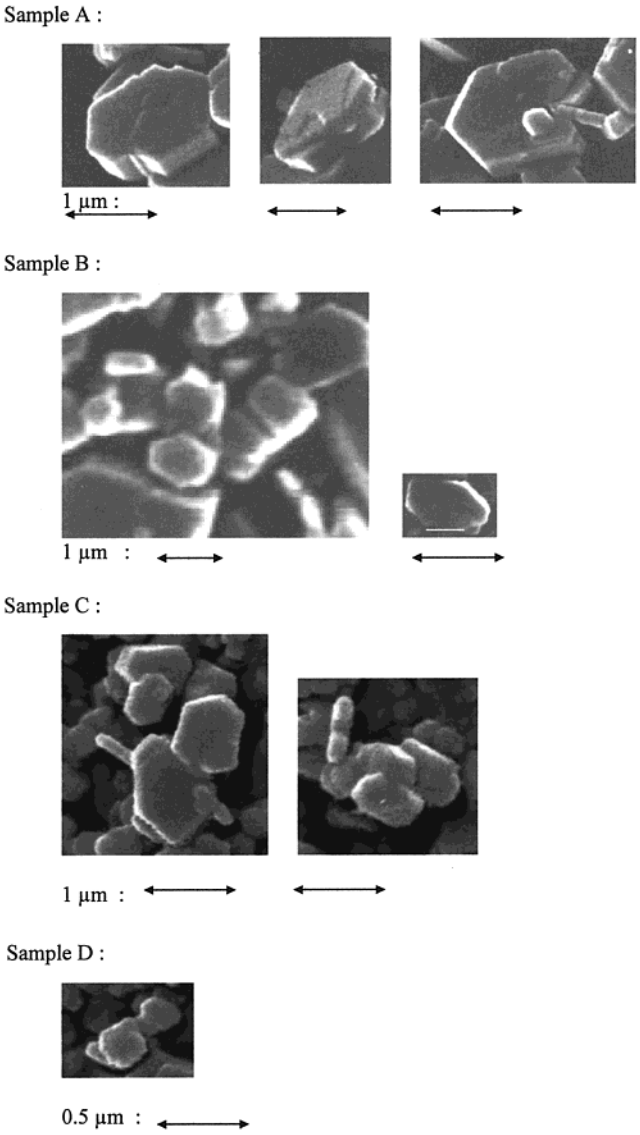

Figure 2. Scanning electron micrographs of our four gibbsite samples

Table 2. Crystal Dimensions Observed by Electronic Microscopy

sample	av size (μm)	est diameter (μm)	est height (μm)
A	1.7 ± 0.2	1.7 ± 0.2	1.7 ± 0.2
B	0.9 ± 0.4	0.9 ± 0.4	0.4 ± 0.1
C	0.5 ± 0.3	0.7 ± 0.2	0.2 ± 0.1
D	0.25 ± 0.05	0.25 ± 0.05	?

The electron micrographs of these four samples show hexagonal shapes, with several "broken" particles (Figure 2). Table 2 gives geometrical parameters estimated for the four samples, although the estimation difficulty increases when the crystal size decreases. Moreover, because of the shapes of the platelets, the crystals tend to settle flat on (001) faces. Consequently, it is easier to give an estimation of a particle diameter than its thickness. However, most particles appear well crystallized and always present well-defined geometrical forms with

(27) Rooksby, H. P. In *The X-ray identification and crystal structures of clay minerals*; Brown, G., Ed.; Mineralogical Society: London, 1972; p 354.

(28) Huneke, J. T.; Cramer, R. E.; Alvarez, R.; Swaify, S. A. *Soil. Sci. Soc. Am. J.* **1980**, *44*, 131.

(29) *X-ray Power Data File;* American Society for Testing Materials: Philadelphia, PA, 1959.

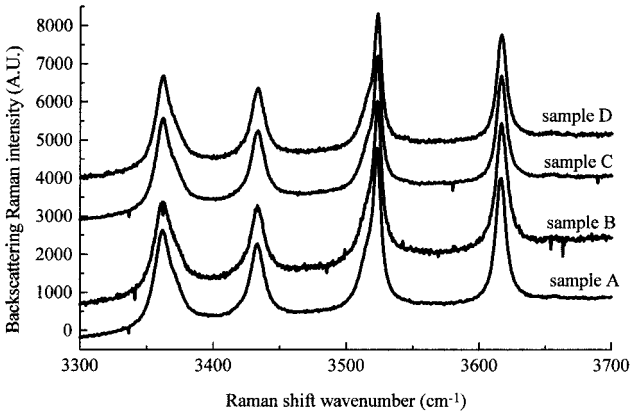

Figure 3. Raman spectra in the OH stretching region. The wavenumbers are those calculated in a vacuum with a precision of ± 1 cm^{-1}.

Table 3. Raman Shift Wavenumbers (cm^{-1}) for Al(OH)$_3$ Crystals[a]

our samples	gibbsite[27]	gibbsite[29]	bayerite[29]	norstrandite[29]
3616	3615	3618/3617	3653	3623
	3544	3566		
3524	3520	3525/24		
3515 (sh)	3510			
	3449 (sh)			
3433	3431	3433	3438 (sh)	
	3424			
3370 (sh)				
3362	3361	3363 (asym)		

[a] The wavenumbers in our work are corrected to give the vibrational wavenumbers in a vacuum for comparison with the infrared data. sh = shoulder.

pronounced angles and often with well-distinguished edge faces separated from basal faces. There are few amorphous particles.

The Raman spectra confirm the gibbsite nature of the particles without any detectable amorphous phases. Four well-resolved components are observed at 3617, 3524, 3433, and 3370 cm^{-1} with two shoulders at 3515 and 3370 cm^{-1}. The relative intensities of the components do not depend significantly on the sample (Figure 3), and no polarization effect is detectable. These Raman shift wavenumbers and spectrum profiles are characteristic of gibbsite and are close to those previously reported in the literature (Table 3).[28,30]

Characterization of the Lateral and Basal Surface Areas from Krypton Adsorption Isotherms. The previous results show that 95% of the four samples are gibbsite crystals. The only differences among the samples lie in the particle sizes and their shape factors, i.e., the area ratios of basal and lateral surfaces. Gas adsorption isotherms provide statistical measurements, on a large particle population, of the specific areas along with information on their shape factors. In the case of kaolinite, previously studied in the literature, the areas of basal and lateral surfaces have been calculated.[24−25,31] We do not discuss here the physical significance of the parameters used to describe the two domains of isotherms. We use the isotherms only to give a quantitative measurement of both domains.

Figure 4 shows an example of a complete adsorption isotherm obtained for sample C. The isotherms of samples A−C each display two distinct adsorption domains without

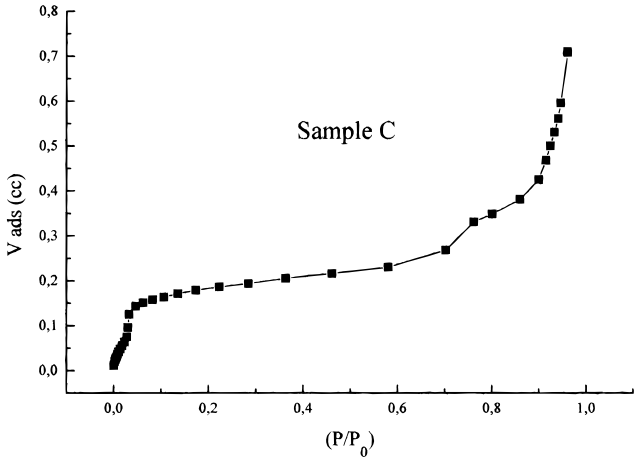

Figure 4. Krypton adsorption isotherm at 77 K for sample C outgassed at 100 °C under a residual pressure of 10^{-6} Pa.

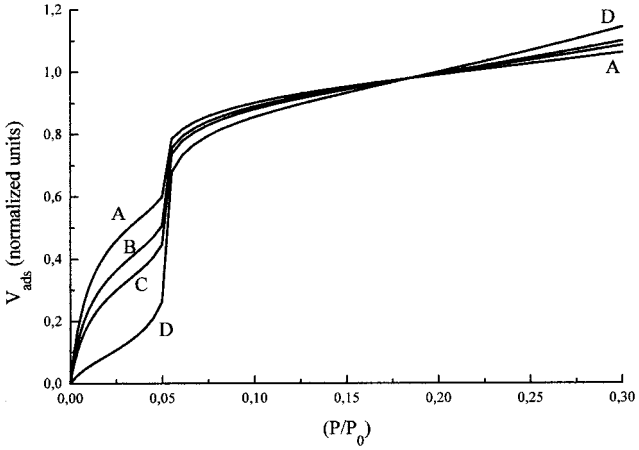

Figure 5. Krypton adsorption isotherms at 77 K for the four samples outgassed at 100 °C under a residual pressure of 10^{-6} Pa for P/P_0 values between 0 and 0.3. The four curves are normalized at $P/P_0 = 0.2$.

microporosity (Figure 5), while the isotherm of the fourth sample does not display so clearly such domains (Figure 5). The total specific surface areas are estimated from these global adsorption experiments (last column of Table 4). Figure 5 displays the domain of low pressures where the two stages of adsorption are clearly shown. To obtain a quantitative description of these isotherms, we applied the derivative isotherm summation (DIS) method previously developed by Villièras et al.[24,25] In this method, the different adsorption domains are assumed to be homogeneous. Consequently, in these domains, the usual adsorption equations of Langmuir and BET, along with their extensions taking into account lateral interactions between admolecules, are used.

In the Langmuir hypothesis, the isotherms are described by

$$\Theta = \frac{Ce^{u}}{1 + Ce^{u}} \qquad (4)$$

where $u = \ln(P/P_s)$ and Θ is the fractional coverage of adsorption sites having the same adsorption energy. The statistical thermodynamic description of the Langmuir isotherm assumes that the adsorbed molecules differ from gaseous ones in that their potential energy and local partition function have been modified and that, instead of possessing normal translational motion, they are confined to localized sites without any interaction between

(30) Rodgers, K. A. *Clay Miner.* **1993**, *28*, 85.
(31) Cases, J. M.; Cunin, P.; Grillet, Y.; Poinsignon, C.; Yvon, J. *Clay Miner.* **1986**, *21*, 55.

Table 4. Fitting Values for the Derived Isotherms of the Four Gibbsite Samples

sample	Langmuir isotherm parameters		lateral specific area (m^2/g)	BET isotherm parameters			basal specific area (m^2/g)	total specific surface area (m^2/g)
	u_{max}	C		u_{max}	C	a		
A	−4.7	110	1	−2.9	3	3.60	0.5	1.5 ± 0.2
B	−4.75	115	2	−2.85	2.7	3.75	2	4 ± 0.3
C	−4.7	110	2.5	−2.9	2.9	3.70	3.5	6 ± 0.5
D	−4.8	120	7.5	−2.85	2.9	3.6	63	70 ± 5

adjacent molecules but with an adsorption energy Q. The partition function for the gas phase can be written as

$$Z^{gas} = Z^{gas}_{trans} Z^{gas}_{internal}$$

and that for the adsorbed phase as

$$Z^{surf} = Z^{surf}_{site} Z^{surf}_{internal} \exp(Q/RT)$$

where the inclusion of the term $\exp(Q/RT)$ means that Z^{surf} is referred to the gaseous state. The complete partition function may be obtained by multiplying Z^{surf} by the number of distinguishable ways of placing N molecules on S sites.[32] Moreover, if the approach of Fowler and Guggenheim[32] is followed, the lateral interaction may be taken into account in eq 1. If the lateral interaction energy is β, the added energy of adsorption is $m\beta\Theta/2$, where each site has m neighbors. The added differential energy of adsorption is just $m\beta\Theta$, which will be noted in the following $\omega\Theta$. As long as the lateral interactions may be neglected, the derivatives of eq 4 are

$$\frac{d\Theta}{du} = \Theta(1-\Theta) = \frac{Ce^u}{(1+Ce^u)^2} \tag{5}$$

$$\frac{d^2\Theta}{du^2} = \frac{Ce^u(1-Ce^u)}{(1+Ce^u)^3} = \Theta(1-\Theta)(1-2\Theta) \tag{6}$$

The inflection point of an isotherm is obtained at $Ce^u = 1$ where $\Theta = {}^1/_2$. The position of this point may be determined experimentally from the first derived curve at u_{max} (or P_{max}):

$$\Theta_{max} = {}^1/_2 \qquad C = (P_S/P_{max}) = \exp(-u_{max}) \tag{7}$$

The value of the first-derivative curve at this point is $(d\Theta/du)u_{max} = {}^1/_4$. The determination of this experimental point gives the constant C and the volume of gas required for the monolayer formation $V_m = 4(dV_{ads}/du)u_{max}$. If now one takes into account the lateral interactions, the expressions for isotherms can be written as

$$\Theta = \frac{Ce^{a\Theta}e^u}{1+Ce^{a\Theta}e^u} \qquad a = \omega/kT \tag{8a}$$

$$\frac{d\Theta}{du} = \frac{\Theta(1-\Theta)}{1-a\Theta(1-\Theta)} \tag{8b}$$

$$\frac{d^2\Theta}{du^2} = \frac{\Theta(1-\Theta)(1-2\Theta)}{[1-a\Theta(1-\Theta)]^3} \tag{8c}$$

Equation 8a is the Bragg−Williams−Temkin isotherm. The $d\Theta/du$ curve displays its maximum at $\Theta = {}^1/_2$. Thus C and u_{max} are related by

$${}^1/_2 = \frac{Ce^{u_{max}}}{\exp(-a/2) + Ce^{u_{max}}} \qquad C = \exp(-u_{max} - a/2)$$

From the determination of u_{max} and a correct adjustment of the parameter a, with respect to the shape of the experimental derivative curve, C and the theoretical height of the derivative curve are calculated:

$$\left(\frac{d\Theta}{du}\right)_{u_{max}} = \frac{1}{4-a}$$

Now, if the affinity of the adsorbate for the surface is such that $C < 1000$, the adsorption in the second layer starts effectively before that in the first layer is completed.[24] The BET theory may then be used:

$$\Theta = \frac{Ce^u}{(1-e^u)[1+(C-1)e^u]} \tag{9a}$$

$$\frac{d\Theta}{du} = \frac{[1+(C-1)e^{2u}]Ce^u}{(1-e^u)^2[1+(C-1)e^u]^2} \tag{9b}$$

$$\frac{d^2\Theta}{du^2} = \frac{[1-(C-2)e^u + 6(C-1)e^{2u} + (C-1)(C-2)e^{2u} + (C-1)^2e^{4u}]Ce^u}{(1-e^u)^3[1+(C-1)e^u]^3} \tag{9c}$$

The relation between C and u_{max} is given by

$$1 + e^{u_{max}} + (C-1)(e^{-u_{max}} + 6e^{2u_{max}} - e^{3u_{max}}) + (C-1)^2(e^{3u_{max}} + e^{4u_{max}}) = 0$$

In the case of nonnegligible lateral interactions, the following modification is used:

$$\Theta = \frac{Ce^{a\Theta}e^u}{(1-e^u)[1+(Ce^{a\Theta}-1)e^u]} \tag{10a}$$

$$\frac{d\Theta}{du} = \frac{Ce^{a\Theta}e^u + \Theta e^u[1-(Ce^{a\Theta}-1)(1-2e^u))}{(1-e^u)\{1+[Ce^{a\Theta}(1+a\Theta)-1]e^u\} - aCe^{a\Theta}e^u} \tag{10b}$$

Thus, the experimental values of a and C are determined step by step in a fitting procedure. First a and C values are fixed and Θ is computed according to the previous equations. Second, $d\Theta/du$ is computed and u_{max} is determined; then C is corrected and checked. Third, after the adjustment of the C value, if the calculated shape of the isotherm is still different from the experimental shape, the parameter a is modified and C is calculated again. Figure 6 gives an example of the application of the DIS method to the isotherm of sample C. Table 4 shows the numerical values obtained for the four samples. Each isotherm is fitted to the sum of a Langmuir isotherm without lateral interactions in the lowest pressure range and a BET isotherm for higher pressures. The less

(32) Adamson, A. W. *Physical Chemistry of Surfaces*, 5th ed.; Wiley-Interscience: New York, 1990.

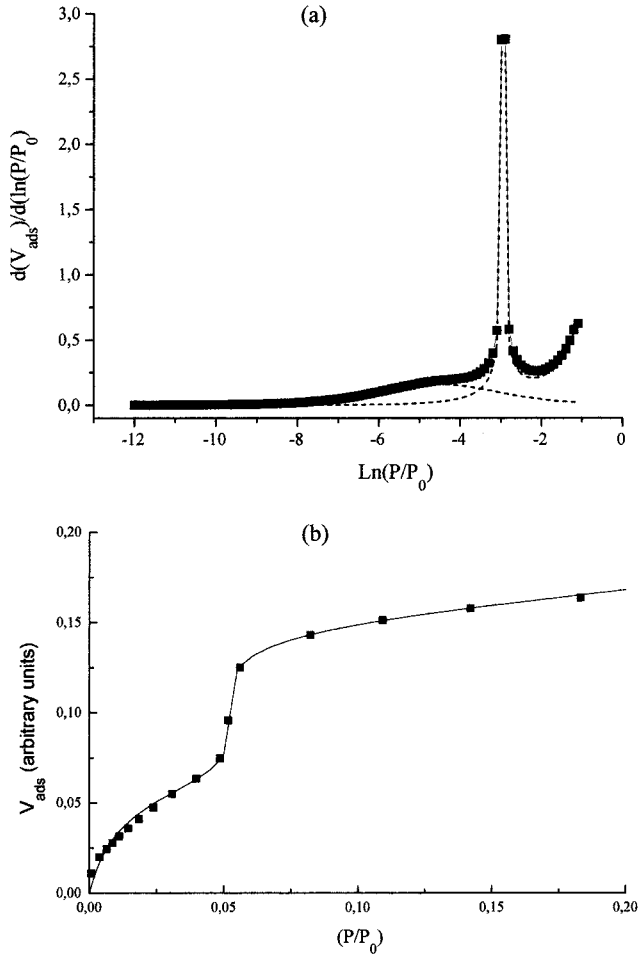

Figure 6. Application of the derived isotherm summation (DIS) method to sample C. (a) Fitting of the derived isotherm, with two components: a Langmuir isotherm at low pressure without any lateral interaction and a BET isotherm at highest pressures with a strong lateral interaction. (b) Comparison of the isotherm calculated by the DIS method with values of $C = 110$, $u_{max} = -4.7$, and $a = 0.02$ for the Langmuir isotherm part and $C = 2.9$, $u_{max} = -2.9$, and $a = 3.7$ for the second part (solid line) with the experimental points (square dots).

energetic domain is assigned to the basal surface, while the more energetic domain is assigned to the adsorption of krypton on edge faces. The only difference among the four samples lies in the relative values of the lateral specific areas (Table 4). The increase of the total specific area is essentially due to the increase of the basal surface. For instance, when the total area is multiplied by a factor of 4.5, the basal area is multiplied by 120 while the lateral areas are multiplied by only ~8. Thus, when the area increases, the heights of the particles decrease more than their diameters, in good agreement with the observations of electron microscopy (Table 2).

Infrared Spectra. Figure 7 displays the overall diffuse reflectance infrared spectrum of sample D, and Figure 8 compares the transmittance spectra of the four gibbsite samples in the OH stretching region. In contrast with the Raman spectra (Figure 3), for which the four vibrational spectra are similar, the infrared spectra between 3000 and 4000 cm^{-1} show important differences among the four samples. Whereas the spectra display four similar components at 3620 ± 1, 3528 ± 0.5, 3394 ± 1, and 3377 ± 3 cm^{-1}, an additional band appears in each spectrum between 3445 and 3460 cm^{-1} with an increasing intensity from sample A to sample D and a concomitantly increasing wavenumber (Figure 8). Because the gibbsite particles

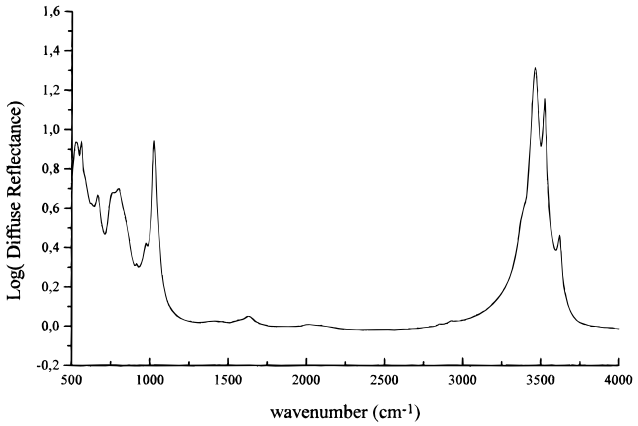

Figure 7. Diffuse reflectance infrared spectrum of the gibbsite D sample mixed at 4% by weight with KBr.

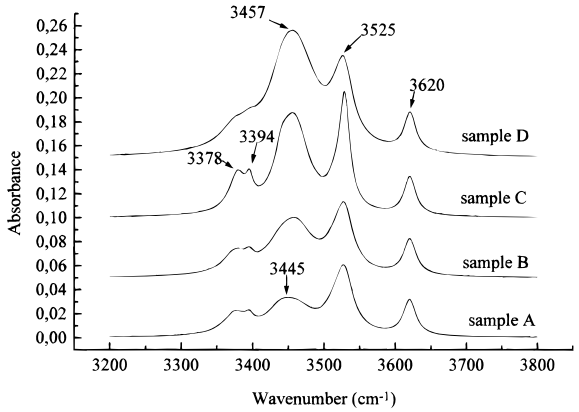

Figure 8. Transmission infrared spectra of the four gibbsite samples, showing the OH stretching modes. The spectra were obtained with pellets each containing a mixture of 0.4% by weight of a gibbsite sample with KBr. The cautions exercised in recording the spectra are discussed in the text.

were anisotropic, we verified that this component at 3445/3460 cm^{-1} was not dependent on the orientation of a pellet relative to the infrared beam. For each orientation, all the relative intensities of the components of the spectra were maintained. Moreover, the intensity of the band at 3620 cm^{-1} was a nearly linear function of the masses of gibbsite in the pellets and was not dependent on the sample (Figure 9). The intensities of the other components at 3528, 3394, and 3377 cm^{-1} were difficult to measure directly and to quantify because the intensity changes of the component at 3450 cm^{-1} strongly perturbed these neighboring components. A decomposition method was used to integrate the intensity of each infrared component. All the decomposition parameters were adjusted step by step to fit all the spectra with the same parameter set. The procedure was to decompose first the infrared spectrum of sample A into seven components at 3378, 3395, 3430, 3450, 3515, 3528, and 3620 cm^{-1} with variable widths at half-height and with small shifts of the components. This component set, which fit closely the spectrum of sample A, was injected into the fitting of the spectrum of sample B. If the decomposition of this spectrum using the seven previous components without changing the wavenumbers and the full widths at half-height is achieved merely by adjusting of the area of each component, then the parameter set is used for the subsequent decomposition, or else some parameters are changed by the user and injected once more to decompose with a good agreement the previous spectra as well as the current spectrum. This procedure, repeated for the subsequent spectra, converges

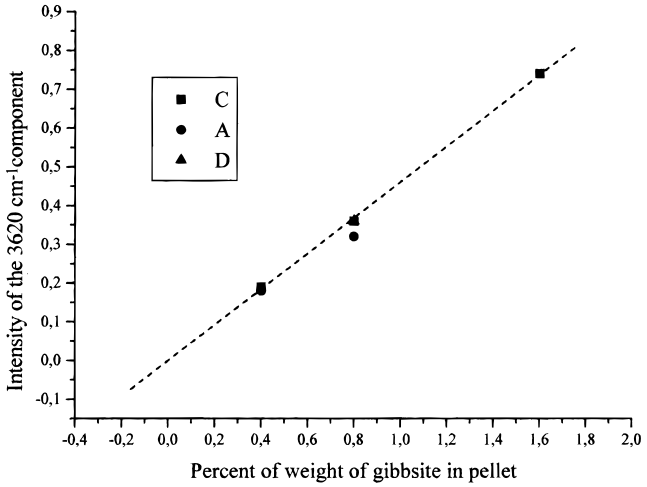

Figure 9. Intensity of the component at 3620 cm^{-1} versus the mass of sample in the pellet. Each intensity given in this figure was measured as the height of the signal in absorbance units. This measurement is easy and does not need any decomposition of spectra. However, the integrated intensities also show a linear dependence on the mass.

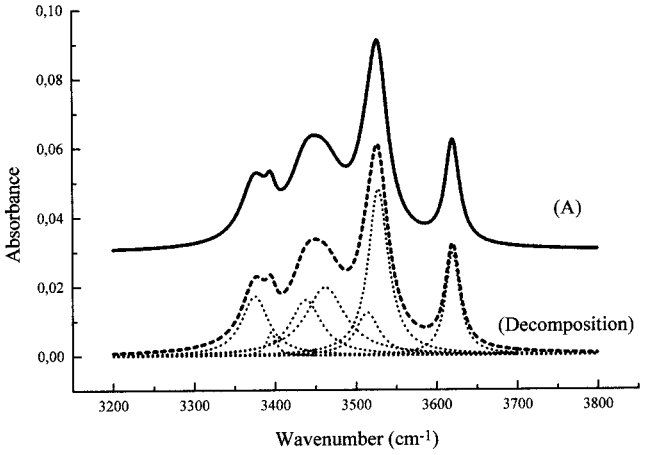

Figure 10. Decomposition results for sample A, with the components discussed in the text.

Table 5. The Seven Lorentzian Components of the Infrared Spectra of the Gibbsite Samples

wavenumber (cm^{-1})	width (cm^{-1})	integrated absorbance (cm^{-1}) obtained with pellets containing 200 mg of sample at 0.4% by weight in KBr	$\int \epsilon\, d\sigma$ (km mol^{-1})[a]
3620 ± 0.5	18 ± 3	9 ± 1	14 ±2
3527 ± 2	25 ± 5	23 ± 4	37 ± 6
3514 ± 5	25 ± 5	5 ± 1	8 ± 2
3461 ± 3	60 ± 10	18−110	
3438 ± 3	35 ± 5	7.5 ± 0.5	12 ± 1
3394 ± 2	20 ± 2	2 ± 0.8	3 ± 1
3375 ± 1	30 ± 2	11 ± 1	18 ± 2

[a] The value of $\int \epsilon\, d\sigma$ were calculated according to the Beer−Lambert absorption law hypothesis from the integrated intensities divided by 3 (for 3 mol of hydroxide in $Al(OH)_3$).

quickly enough for all four samples. Figure 10 shows, for example, the decomposition of the spectrum of sample A, and Table 5 gives the final values of these parameters with the integrated intensity of each component. Only the component at 3461 cm^{-1} varies strongly from sample A to sample D. This component is displayed in the difference spectrum between samples D and A (Figure 11), which shows a broad band at 3461 cm^{-1} with a possible

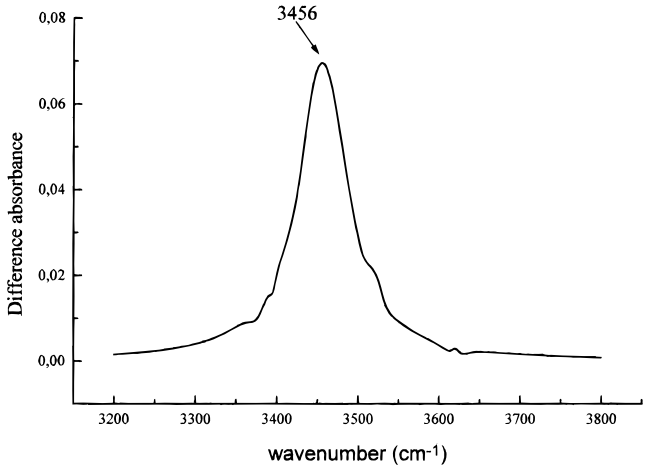

Figure 11. Difference spectrum between samples D and A, obtained by the subtraction (spectrum of sample D) − (1.096 × spectrum of sample A), without another treatment.

shoulder at about ∼3520 cm^{-1}. Figure 12 shows the variation of the normalized integrated intensity of this component versus the total specific surface area, the specific basal area, and the specific lateral area. The normalization is obtained by dividing the intensity of the component at 3461 cm^{-1} by the intensity of the component at 3620 cm^{-1}, which is assumed to be proportional to the mass of gibbsite (Figure 9). The plot in Figure 12c shows clearly that the component at 3461 cm^{-1} is roughly proportional to the lateral area. The values of $\int \epsilon\, d\sigma$ in km mol^{-1} given in Table 5 are partial absorption coefficients of a mean hydroxide calculated according to the Beer−Lambert absorption law hypothesis from the integrated decadic absorbance divided by 3 (for the 3 mol of hydroxide in $Al(OH)_3$). The value of $\int \epsilon\, d\sigma$ for the 3461 cm^{-1} component was not computed because this component cannot be assigned to vibrational modes of bulk hydroxides. Thus the total mean integrated decadic absorption coefficient of a bulk hydroxide of gibbsite is 92 km mol^{-1}. Each individual value of Table 5 should be related to each hydroxide family, and consequently a new complete assignment for each component should be discussed in light of the fact that the component 3461 cm^{-1} is not a vibrational mode of the bulk hydroxides. This work will be soon published.

The component at 3461 cm^{-1} should involve both species $AlOH_2^{1/2+}$ and $AlOH^{1/2-}$ which are probably interacting either with each other as

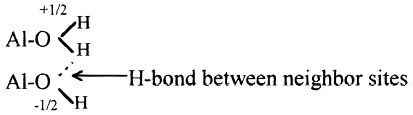

or with residual water molecules as

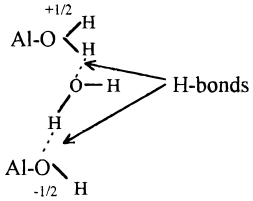

Other more complicated forms may be proposed between more hydroxides of different layers. A study of hydrogen/deuterium exchange was conducted for a pure sample of gibbsite D with a diffuse reflectance accessory working

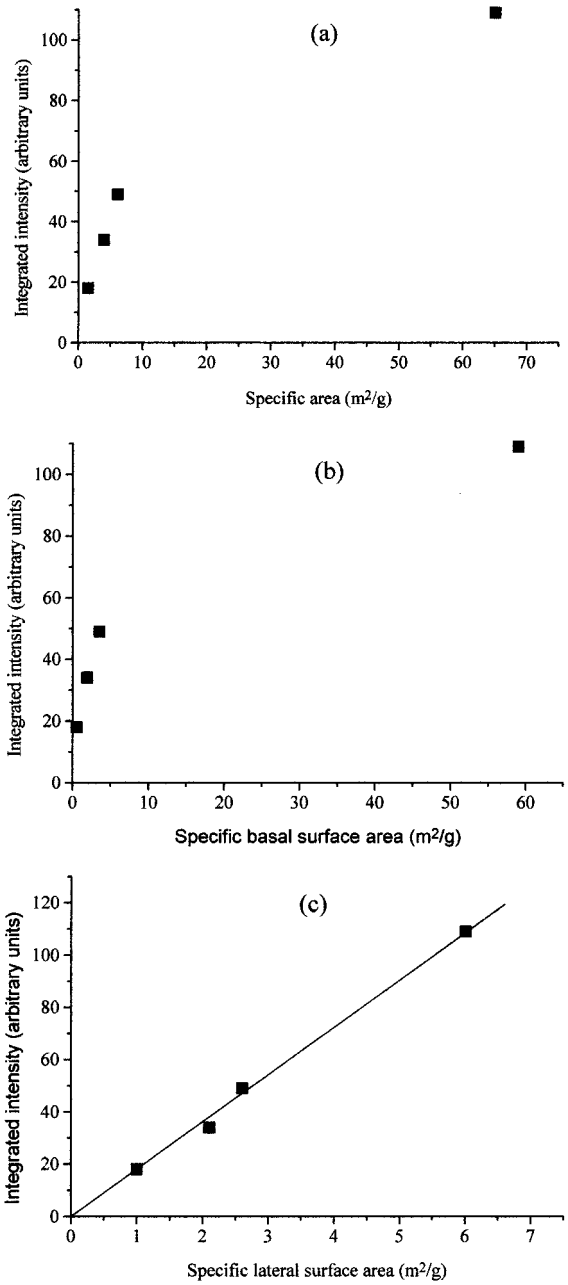

Figure 12. Integrated intensity of the 3461 cm^{-1} component normalized with respect to the 3620 cm^{-1} component versus: (a) the total specific areas of the samples, (b) the basal surface specific areas of the samples, and (c) the lateral surface specific areas of the samples.

under a controlled pressure or vacuum. A diffuse reflectance study of a pure sample results in the deformation of the shapes of the intense absorption bands; however, it qualitatively shows the appearance and the increase of a small component. Figure 13 displays the spectrum obtained after deuteration of a pure powder sample of gibbsite D under a pressure of 10^{-2} mbar in the range 2900−2400 cm^{-1}. A broad asymmetric band appears

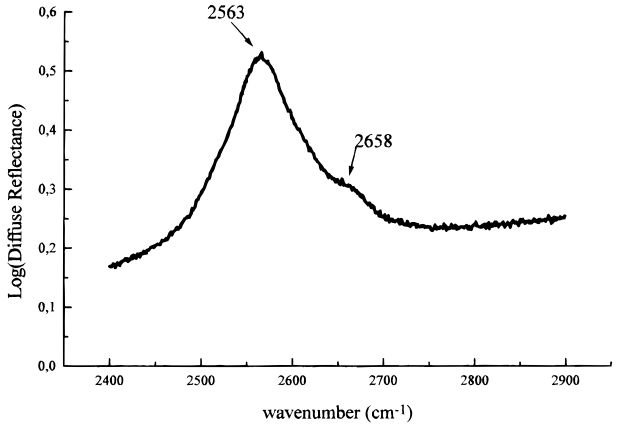

Figure 13. Diffuse reflectance spectrum, between 2400 and 2900 cm^{-1}, obtained for a pure powder of sample D, under a pressure of about 10^{-2} mbar, after a rapid OH/OD exchange under a low pressure of D_2O.

centered at 2563 cm^{-1}, with a shoulder at 2658 cm^{-1}. The 2563 cm^{-1} band corresponds to the 3461 cm^{-1} in the OH stretching region with an isotopic ratio of about 1.35. This experiment demonstrates that the exchange is faster for this OH population than for the hydroxides characteristic of the crystalline structure of the gibbsite. The shoulder at 2658 cm^{-1} could correspond to the wavenumbers 3580−3590 cm^{-1} in the OH region. This last absorption may be the mode for the beginning of the deuterium/hydrogen exchange of bulk OH groups (bands at 3620 and 3525 cm^{-1}) or other modes of superficial hydroxides which are not clearly displayed between 3400 and 3600 cm^{-1} because of the overlaps of the components of the vibrating modes of the bulk OH groups. In any case, the asymmetrical component at 3461 cm^{-1} (or 2563 cm^{-1} in the OD spectral region) is a spectral fingerprint of the lateral hydroxide species. Finally, this vibrational mode, which displays a strong variation in the dipolar moment, is not shown in the Raman spectra (Figure 3) and consequently results in a very weak variation of the polarizability.

Conclusion

For crystallized gibbsite samples with well-defined lateral and basal planes, the intensity of the infrared component at ∼3460 cm^{-1} is linearly related to the lateral surface area measured by gas adsorption isotherms. To avoid any interference from physically adsorbed water on the pellets, great care should be exercised when the infrared spectra are recorded in the transmission mode. The band at 3460 cm^{-1} is not easily assigned to a specific vibrational mode of one specific species, but it is related to the species $AlOH_2^{1/2+}$ and $AlOH^{1/2-}$ present with or without hydrogen-bonded water molecules on the edge planes. This strong infrared component is not displayed in Raman spectra. Consequently, we can conclude that this absorption is due to a large transition dipolar moment and that the variation in polarizability is very weak.

LA000098V